Acta Materialia 130 (2017) 297–309

Contents lists available at ScienceDirect

Acta Materialia

journal homepage: www.elsevier.com/locate/actamat

Full length article

In situ synchrotron high-energy X-ray diffraction study of microscopic deformation behavior of a hard-soft dual phase composite containing phase transforming matrix

Junsong Zhang [a, b], Shijie Hao [c], Daqiang Jiang [c], Yong Huan [d], Lishan Cui [c, *], Yinong Liu [a, **], Hong Yang [a], Yang Ren [e]

[a] School of Mechanical and Chemical Engineering, The University of Western Australia, Crawley, WA 6009, Australia
[b] Institute for Advanced Materials, Jiangsu University, Zhenjiang, 212013, China
[c] Department of Materials Science and Engineering, China University of Petroleum-Beijing, Changping, Beijing, 102249, China
[d] State Key Laboratory of Nonlinear Mechanics (LNM), Institute of Mechanics, Chinese Academy of Sciences, Beijing, 100190, China
[e] X-ray Science Division, Argonne National Laboratory, Argonne, IL 60439, USA

ARTICLE INFO

Article history:
Received 25 January 2017
Received in revised form
19 March 2017
Accepted 21 March 2017
Available online 24 March 2017

Keywords:
Composite
Mechanical behavior
High-energy X-ray diffraction
Martensitic transformation
TiNi

ABSTRACT

This study explored a novel intermetallic composite design concept based on the principle of lattice strain matching enabled by the collective atomic load transfer. It investigated the hard-soft microscopic deformation behavior of a Ti_3Sn/TiNi eutectic hard-soft dual phase composite by means of in situ synchrotron high-energy X-ray diffraction (HE-XRD) during compression. The composite provides a unique micromechanical system with distinctive deformation behaviors and mechanisms from the two components, with the soft TiNi matrix deforming in full compliance via martensite variant reorientation and the hard Ti_3Sn lamellae deforming predominantly by rigid body rotation, producing a crystallographic texture for the TiNi matrix and a preferred alignment for the Ti_3Sn lamellae. HE-XRD reveals continued martensite variant reorientation during plastic deformation well beyond the stress plateau of TiNi. The hard and brittle Ti_3Sn is also found to produce an exceptionally large elastic strain of 1.95% in the composite. This is attributed to the effect of lattice strain matching between the transformation lattice distortion of the TiNi matrix and the elastic strain of Ti_3Sn lamellae. With such unique micromechanic characteristics, the composite exhibits high strength and large ductility.

1. Introduction

Conventional metallic materials generally have relatively large plasticity due to having massive population of microstructural defects, which facilitate plastic deformation. By the same argument these structural defects render the materials relatively low strength, thus low load-bearing capability, by allowing easy plastic deformation. Some intermetallic compounds and ceramic compounds are able to exhibit higher strengths owing to their stronger interatomic bonding. Low-dimension materials, e.g., nanoparticles, nanowires, and nanoribbons, have been shown to exhibit exceptionally high strength intrinsic to the solids [1–3], generally due to the lack of structural defects in their crystal. Once again, for the same reason these materials present low ductility due to the absence of effective plastic deformation mechanisms. This has been an intrinsic contradiction and dilemma in materials design for high strength and high ductility.

One possible approach is to combine the attributes of ductile materials and high-strength materials in one composite, and indeed many hard-soft dual phase composites have been designed in the past [4–12]. A common configuration of hard-soft dual phase composites consists of a hard reinforcement embedded in a continuous soft and ductile metallic matrix [5–7]. The hard reinforcement generally serves as the primary load bearer for strength, and the continuous soft and ductile matrix plays the role for load transfer and distribution [5–7].

Whereas the concept seems to be simple and straight forward, the practice is challenging. The essence of such composite design is to achieve synergy between the properties of the two components,

* Corresponding author.
** Corresponding author.
E-mail addresses: lscui@cup.edu.cn (L. Cui), yinong.liu@uwa.edu.au (Y. Liu).

http://dx.doi.org/10.1016/j.actamat.2017.03.052
1359-6454/

as opposed to "antergy" (antonym to synergy), and that is where the scientific challenge lies. In conventional hard-soft dual phase metallic matrix composites, the deformation mechanism of the soft phase is primarily dislocation slip [5–7]. Extensive knowledge has been established of the mechanical behavior of conventional metallic matrix composites [13–18]. In the early stage of elastic deformation, load partition between the two components occurs following the rule of mixture. When plastic deformation commences in the matrix, load transfer from the matrix to the reinforcement occurs [16–18], allowing higher load bearing capability of the composite. However, the highly localized lattice distortion of dislocation in conventional metals easily triggers large strain mismatch at the interface, which in turn results in local stress concentration and causes premature local failure of the reinforcement. Consequently, the intrinsic mechanical properties of reinforcement can not be achieved in this conventional composite design strategy [16–18]. This drawback hinders the further improvement of mechanical properties of the composite.

In this work, we applied the recently established nanoscience knowledge at the lattice level to bulk composite design to overcome this challenge. Recently, it is demonstrated that nano reinforcement materials in composites can exhibit ultra-large elastic strains, 5–10 times larger than in bulk form or in conventional metal matrix composites, when embedded in a martensitic phase transforming matrix [19,20]. This unique phenomenon is attributed to the principle of lattice strain matching at the sub-nanometric scale between the transformation lattice distortion of the martensitic matrix and elastic strains of the nanoinclusions. The uniform (and generally lower, <10%) lattice distortion of a martensitic transformation is much easier to coordinate at the interface with the reinforcement than the highly localized lattice strains at a dislocation slip band. This helps to prevent high local stress concentration and assure a relatively uniform stress distribution, thus preventing the premature failure of the rigid component and assuring collective atomic load transfer. This discovery presents a breakthrough to the deadlock of limited elastic strains of nanomaterials in conventional metal matrix composites [19,20] and a new opportunity to design and engineer superior metal matrix composites of exceptional mechanical prowess.

This unique design concept based on lattice strain matching has been demonstrated in a Nb/TiNi nanocomposite system [21]. The composite consists of a polycrystalline TiNi matrix embedded with Nb nanowires of 20–60 nm in diameter all aligned along the axial direction of the composite wire [19,20]. The Nb nanowires in this composite achieved a maximum elastic strain of 6.5%, implying a strength (load bearing) contribution of ~5600 MPa the nanowires within the composite [19,20]. The near perfect axial alignment, the highly dense and uniform distribution and the very large length-to-diameter aspect ratios of the nanowires make the composite a near perfect parallel configuration system in mechanics, i.e. an iso-strain model. Such parallel connection structure facilitates effective lateral load transfer from the matrix to the nanowires, leading to the achievement of ultra-large elastic strains of the nanowires and consequently the high strength of the composite.

Whereas the fore-mentioned Nb/TiNi nanowire composite has proven to be effective in harnessing the exceptional intrinsic properties of the metallic nanowires in composite, the same concept is yet to be validated in other composite structures, such as nanoinclusions in forms other than wires and nanoinclusions that are less orderly distributed within the matrix. Such knowledge is essential for designing and developing metallic composites of exceptional properties based on the lattice strain matching principle. In this work, we investigated the microscopic deformation mechanism of a eutectic Ti_3Sn/TiNi lamellar composite. The composite provides a unique micromechanical system with distinctive deformation behaviors and mechanisms from the two components, with the soft TiNi matrix deforming in total compliance via martensite variant reorientation and the hard Ti_3Sn lamellae deforming predominantly via rigid body rotation as well as elastic deformation.

2. Experimental procedure

A 1.5 kg alloy ingot with a nominal composition of $Ti_{57}Ni_{35}Sn_8$ (at. %) was prepared by arc melting in a water-cooled copper hearth in an argon atmosphere. Commercial purity Ti (99.99 wt %), Ni (99.99 wt %) and Sn (99.99 wt %) were used as raw materials. The ingot was melted five times in the furnace to obtain chemical composition homogeneity. The composition of the alloy was chosen to conform to a eutectic solidification between TiNi and Ti_3Sn. The morphology of the composite ingot was characterized using a FEI-200F scanning electron microscope (SEM) operated at 20 kV. The microstructure and the local chemical compositions of the composite ingot were analyzed by means of X-ray energy dispersive spectroscopy (EDS) using a FEI Tecnai G2 F20 transmission electron microscope (TEM). Differential scanning calorimetry (DSC) measurement was conducted using a TA INST2910 differential scanning calorimeter with a heating/cooling rate of 10 °C/min to characterize the transformation behavior of the TiNi matrix. The mechanical properties of the composite were tested in compression using a servo-hydraulic materials testing system (MTS 810) at room temperature at a strain rate of 5×10^{-4} s^{-1}. Cylindrical compression samples of $\varphi 5 \times 10$ mm in dimension were prepared according to American Society for Testing and Materials (ASTM) standards.

In situ synchrotron high-energy X-ray diffraction (HE-XRD) measurements were used to study the deformation mechanisms of the composite during compression. A schematic set-up of the measurement is shown in Fig. 1. Experiments were performed on beamline 11-ID-C at the Advanced Photon Source, Argonne National Laboratory, USA. High-energy X-rays with an energy level of 115 keV, wavelength of 0.10798 Å and beam size of 0.6×0.6 mm^2 were diffracted in transmission geometry towards a Perkin-Elmer large area detector to obtain two-dimensional (2D) HE-XRD diffraction patterns. One-dimensional (1D) HE-XRD diffraction spectrums were obtained by integrating along specified azimuth angles over a range of ±10°in the 2D HE-XRD diffraction patterns. Gaussian fits were employed to determine the positions and areas of the diffraction peaks. The lattice strain for a particular set of crystal planes is calculated as $|d_{hkl} - d^0_{hkl}|/d^0_{hkl}$, where d^0_{hkl} is the "unstressed" lattice spacing (i.e., the peak position at zero applied stress). The errors of the lattice strain measurements and the relative peak intensity measurements were estimated to be less than 0.05% and 0.02, respectively.

3. Results

3.1. Microstructure of the composite

Fig. 2 shows the structural analysis of the composite created. Fig. 2(a) shows an SEM backscattered electron image of the Ti_3Sn/TiNi composite. The composite has a full eutectic structure of Ti_3Sn (bright) and TiNi (gray) phases. The microstructure contained two distinctive morphologies of eutectic cells and inter-cell regions, apparently resulting from the solidification process. The average eutectic cell size is approximately 5 μm. Fig. 2(b) shows the interior of a eutectic cell at a higher magnification. The average lamella spacing is 300 nm. Within the inter-cell regions the average "spacing" is much larger. The volume fraction of the Ti_3Sn phase is estimated to be about 30% by image analysis. Fig. 2(c) shows a 2D HE-XRD pattern of the composite. It can be seen that the diffraction

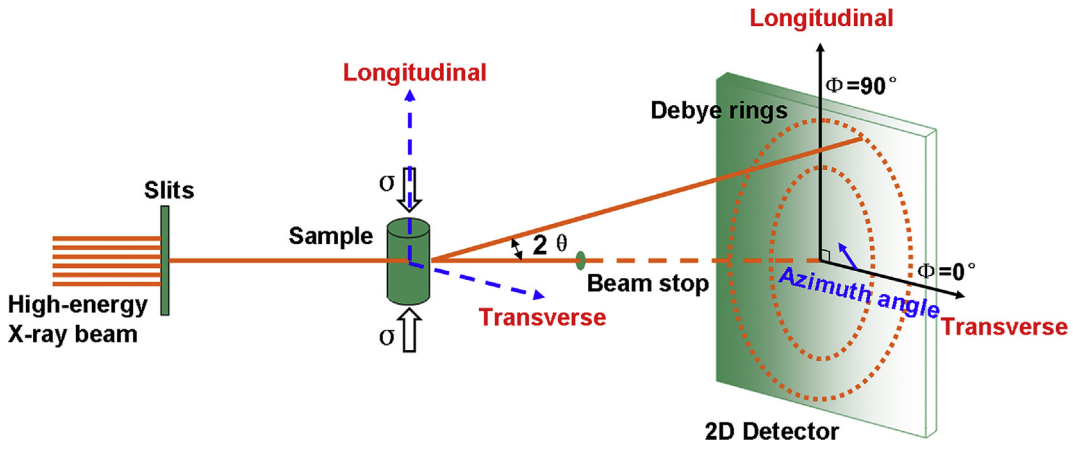

Fig. 1. Schematic illustration of in situ HE-XRD measurements.

rings are continuous and uniform, implying very fine lamella and isotropic eutectic cell microstructure. Fig. 2(d) shows an enlarged view of the area identified by the dashed box in Fig. 2(c) to allow indexing of the diffraction rings. Fig. 2(e) shows a one-dimensional HE-XRD spectrum integrated over the entire 360°. The pattern is fully indexed to the monoclinic $P2_1/m$ TiNi (B19′) phase and the hexagonal $P6_3/mmc$ Ti_3Sn (D019) intermetallic phase.

Fig. 3 shows TEM analysis of the composite. Fig. 3(a) is a TEM bright-field image of the eutectic structure. Selected-area electron diffraction patterns from the bright and gray layers are shown in

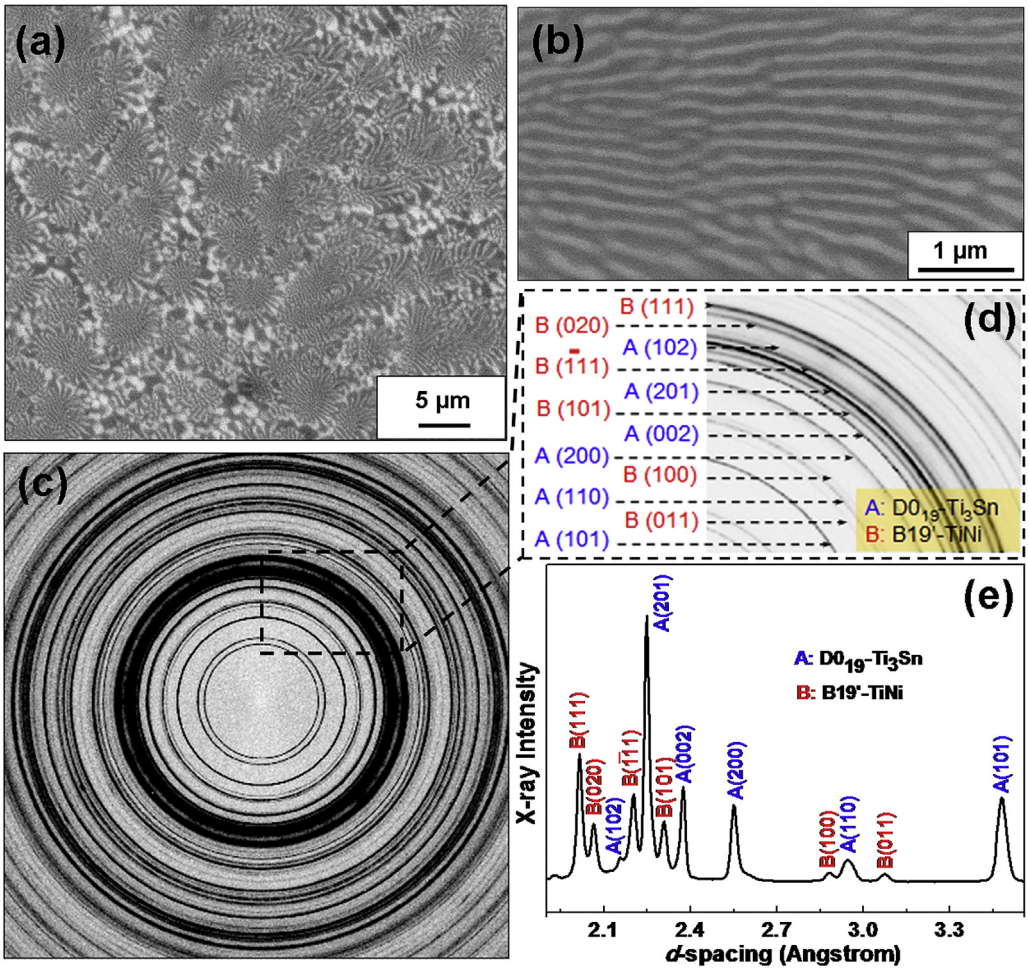

Fig. 2. Structure analysis of the Ti_3Sn/TiNi composite. (a) SEM backscattered electron image of the composite. (b) SEM image of the Ti_3Sn (bright)-TiNi (gray) lamellar structure at a higher magnification. (c) Two-dimensional HE-XRD pattern of the composite. (d) Enlarged view of the boxed area in (c) with the diffraction rings indexed. (e) One-dimensional HE-XRD spectrum integrated at 360° overall of the composite.

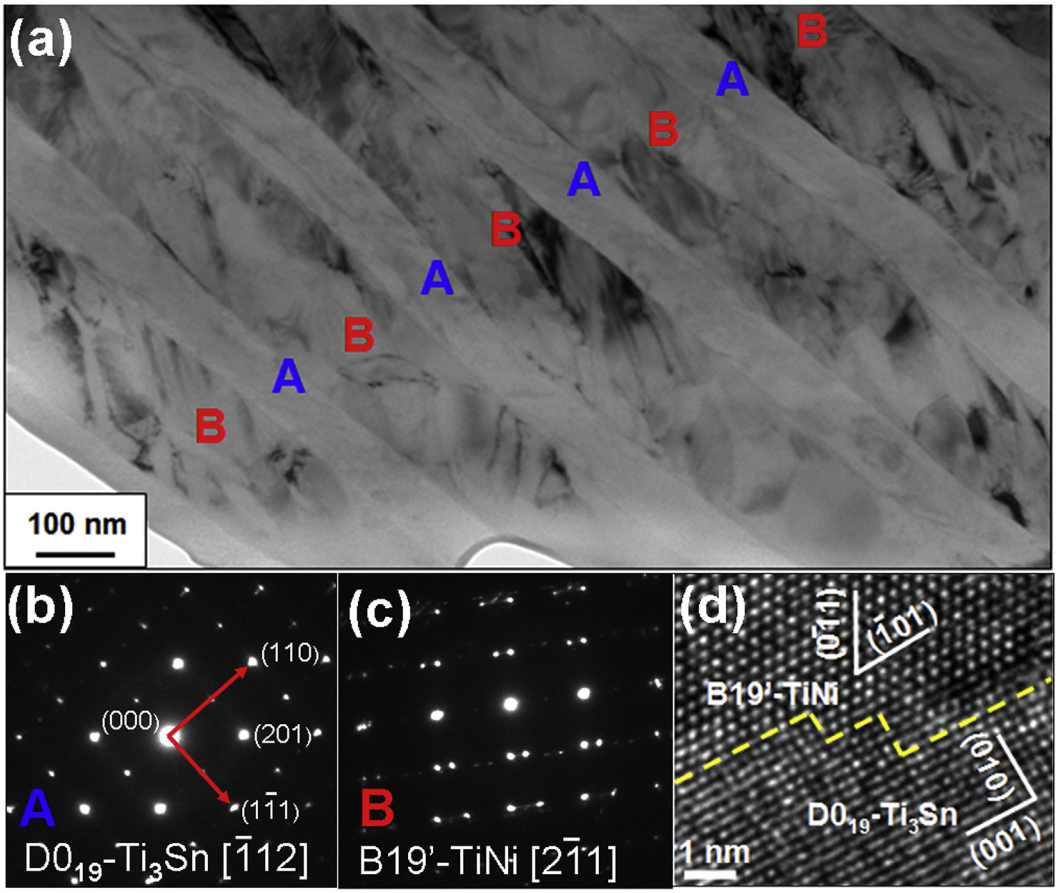

Fig. 3. TEM analysis of the Ti_3Sn/TiNi composite. (a) TEM bright-field image of the composite. A and B regions are Ti_3Sn and TiNi, respectively. (b) and (c) are selected-area electron diffraction patterns of the Ti_3Sn and TiNi lamellae. (d) High-resolution TEM image of the interface between TiNi and Ti_3Sn.

Fig. 3(b) and (c), respectively, confirming the D019-Ti_3Sn (A) structure and the B19′-TiNi (B) structure. The average thicknesses of the Ti_3Sn layers and TiNi layers are approximately 100 nm and 200 nm, respectively. EDS analysis reveals the composition of the Ti_3Sn and TiNi phases in the composite to be $Ti_{74.4}Sn_{21.2}Ni_{4.4}$ (at. %) and $Ti_{49.8}Ni_{49.9}Sn_{0.3}$ (at. %), respectively. Fig. 3(d) shows a high-resolution TEM image of the interface between the two phases, revealing a good structure without third phase inclusions and implying for strong interfacial bonding and efficient load transfer.

3.2. Mechanical behavior of the composite

Fig. 4 shows macroscopic mechanical behavior of the composite. Fig. 4(a) is a compressive stress-strain curve of the Ti_3Sn/TiNi composite at room temperature. The inset in Fig. 4(a) shows a stress-strain curve with several intermediate unloading-reloading cycles. The composite exhibits an ultimate compressive strength of 3 GPa and a large fracture strain exceeding 30%. High strain hardening is also evident. The composite also presents a very low apparent modulus of inelastic deformation during initial loading and a low yielding point. The engineering stress-strain curve of the composite may be divided into four stages (O-A, A-B, B-C and C-D). O-A (<1.2% strain) is the initial "elastic" deformation. A-C (1.2–9.1%) involves martensite variant reorientation [22,23], and C-D is mainly the plastic deformation of the composite.

Fig. 4(b) shows a comparison of the mechanical properties (ultimate compressive strength and fracture strain) of this composite with those of other "hard-soft" dual phase eutectic composites reported in the literature [24–30]. The mechanical properties of this Ti_3Sn/TiNi composite are clearly superior over all other hard-soft dual phase eutectic composites, particularly in terms of the maximum strain prior to rupture.

3.3. In situ HE-XRD characterization

To uncover the microscopic mechanisms of the deformation of the Ti_3Sn/TiNi composite, in situ synchrotron HE-XRD measurements were performed on the composite during compression test. Fig. 5(a) presents the evolution of Ti_3Sn (201) and B19′-TiNi (111) lattice strains along the loading direction as a function of the applied strain. As the applied strain increased, the B19′-TiNi (111) lattice strain initially increased linearly (O-A), reflecting the elastic deformation of the matrix. The lattice strain then remained almost constant over a plateau between 1.2% and 3.9% of the applied strain (A-B), apparently experiencing the process of stress-assisted martensite reorientation. The lattice strain increased rapidly within B-C, indicating the elastic deformation of the fully oriented martensite. The TiNi lattice strain reached 1% at 9.1% of applied strain, beyond which the TiNi lattice strain continued to increase at a much reduced rate to a maximum of 1.1% (C-D). In contrast, the lattice strain of Ti_3Sn increased continuously during deformation, apparently in two stages. The rate of lattice strain increase was fast in stage A-B when the lattice strain of the TiNi matrix was at arrest, but decreased at the end of the plateau of the lattice strain of TiNi (point B), showing an apparent "yield". The maximum elastic strain of Ti_3Sn reached was 1.95%, which is more than six times of the

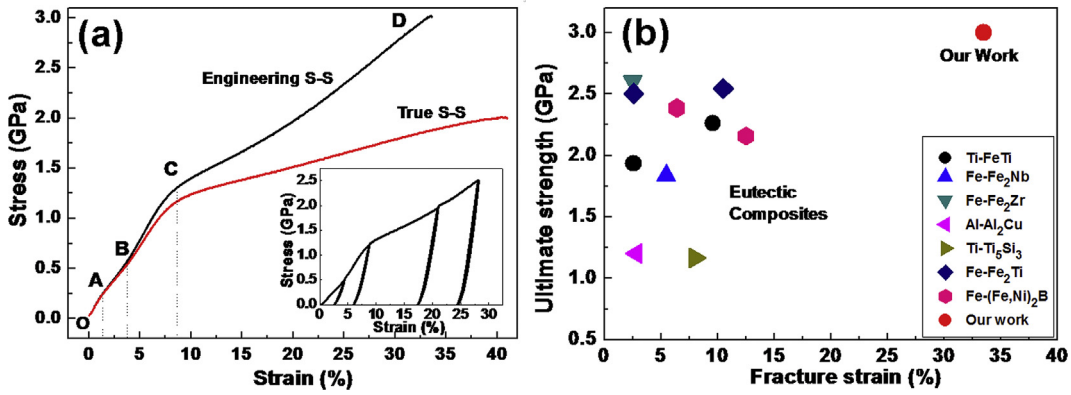

Fig. 4. Mechanical behavior of the Ti_3Sn/TiNi composite. (a) Room temperature compressive stress-strain (S-S) curve of the composite. The red curve shows the true stress-true strain correlation. (b) Comparison of the mechanical properties of the Ti_3Sn/TiNi composite with those of other eutectic composites in which the soft component is a conventional metal (black circle[24], blue uptriangle[25], dark cyan downtriangle[26], magenta lefttri[27], dark yellow righttri[28], navy diamond[29], pink hexagon[30]). (For interpretation of the references to colour in this figure legend, the reader is referred to the web version of this article.)

elastic strain of free-standing Ti_3Sn (approximately 0.3%) reported in the literature [31]. This value is also significantly higher compared to the elastic strains of other hard inclusions (such as nanowires, laminates and particles) embedded in conventional metal matrices that deform by dislocation slip [16–18,32–37], as demonstrated in Fig. 5(b). TiNi is the continuous phase which provides bulk of the inelastic deformation of the composite. Ti_3Sn is the brittle and discontinuous phase which is expected to exhibit negligible plasticity. The elastic lattice strains are also found to be different between TiNi and Ti_3Sn. This is apparently related to load partition between the two phases. TiNi is the soft phase and is more compliant to the external load. Thus during martensite reorientation, load transfer from the soft TiNi matrix to the hard Ti_3Sn occurs [16–18], resulting in higher elastic lattice strains in Ti_3Sn and lower elastic lattice strains in TiNi. Referring to the true stress-strain curve of the composite (Fig. 4(a)) and the lattice strain-applied strain curve shown in Fig. 5(a), it is clear that the apparent strain hardening of the composite mainly stems from the continuous elastic deformation of the hard Ti_3Sn phase.

3.4. Deformation of the soft TiNi component

Fig. 6 shows 1D HE-XRD diffraction spectrums of the soft TiNi component during compressive loading in the longitudinal direction (Fig. 6(a)) and in the transverse direction (Fig. 6(b)), as extracted from the 2D HE-XRD patterns. Upon loading, the diffraction peaks in the longitudinal direction shifted to lower *d*-spacing values, demonstrating compressive elastic deformation in the axial direction (Fig. 6(a)). In contrast, the peaks in the transverse direction shifted to higher *d*-spacing values due to the Poisson's effect. At higher applied strain levels, the diffraction peaks stopped shifting but showed clear broadening with reduced intensity, reflecting increased structural inhomogeneity due to increased defect density upon plastic deformation. In addition, it is seen that the diffraction intensities of the B19′-TiNi (020) and B19′-TiNi (001) peaks decreased whilst that of the B19′-TiNi (111) peak increased in the longitudinal direction (Fig. 6(a)). In the transverse direction (Fig. 6(b)), the opposite behavior is observed, with the exception of the B19′-TiNi (020) diffraction. This reflects martensite variant reorientation in the TiNi matrix during deformation.

The relative peak height intensity, defined as I_{hkl}/I^0_{hkl}, where I^0_{hkl} is the peak height intensity at zero load, is determined for the diffraction peaks in the spectrum. Fig. 6(c) and (d) show the relative peak height intensities of several diffraction peaks as functions of the applied strain in the longitudinal direction and in the transverse direction, respectively. In the longitudinal direction (Fig. 6(c)), the relative peak intensities of (100) and (111) increased whereas those of $(\bar{1}\ 11)$, (020), (011) and (001) decreased. In the transverse

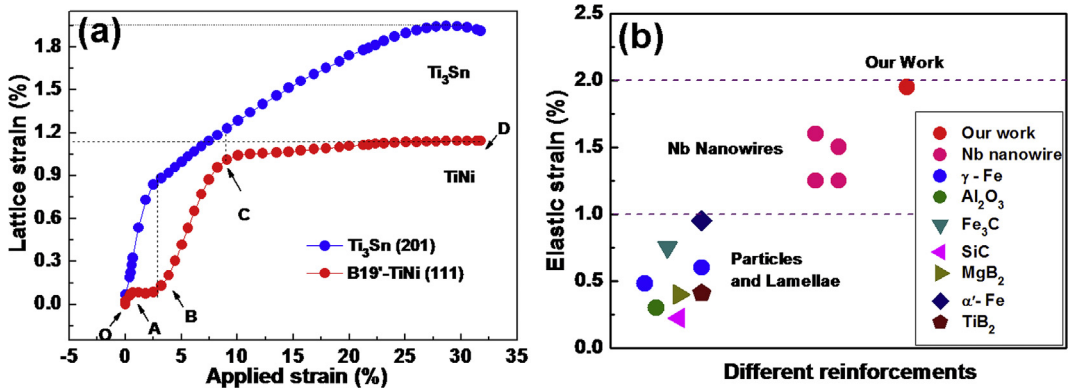

Fig. 5. Microscopic deformation behavior of the Ti_3Sn/TiNi composite. (a) Evolution of B19′-TiNi (111) and Ti_3Sn (201) lattice strains in the longitudinal direction as a function of the applied global strain. Labels "O"-"D" correspond to the labels marked on the stress-strain curve of the composite shown in Fig. 5(a). (b) Comparison of the elastic strain of Ti_3Sn achieved in this Ti_3Sn/TiNi composite with those of other hard inclusions (including nanowires, lamellae, and particles) embedded in conventional metal matrices which deform by dislocation slip [blue circle[32], olive circle[33], dark cyan downtriangle[17], magenta lefttri[34], dark yellow righttri[16], navy diamond[35], wine pentagon[18], pink circle[36,37]]. (For interpretation of the references to colour in this figure legend, the reader is referred to the web version of this article.)

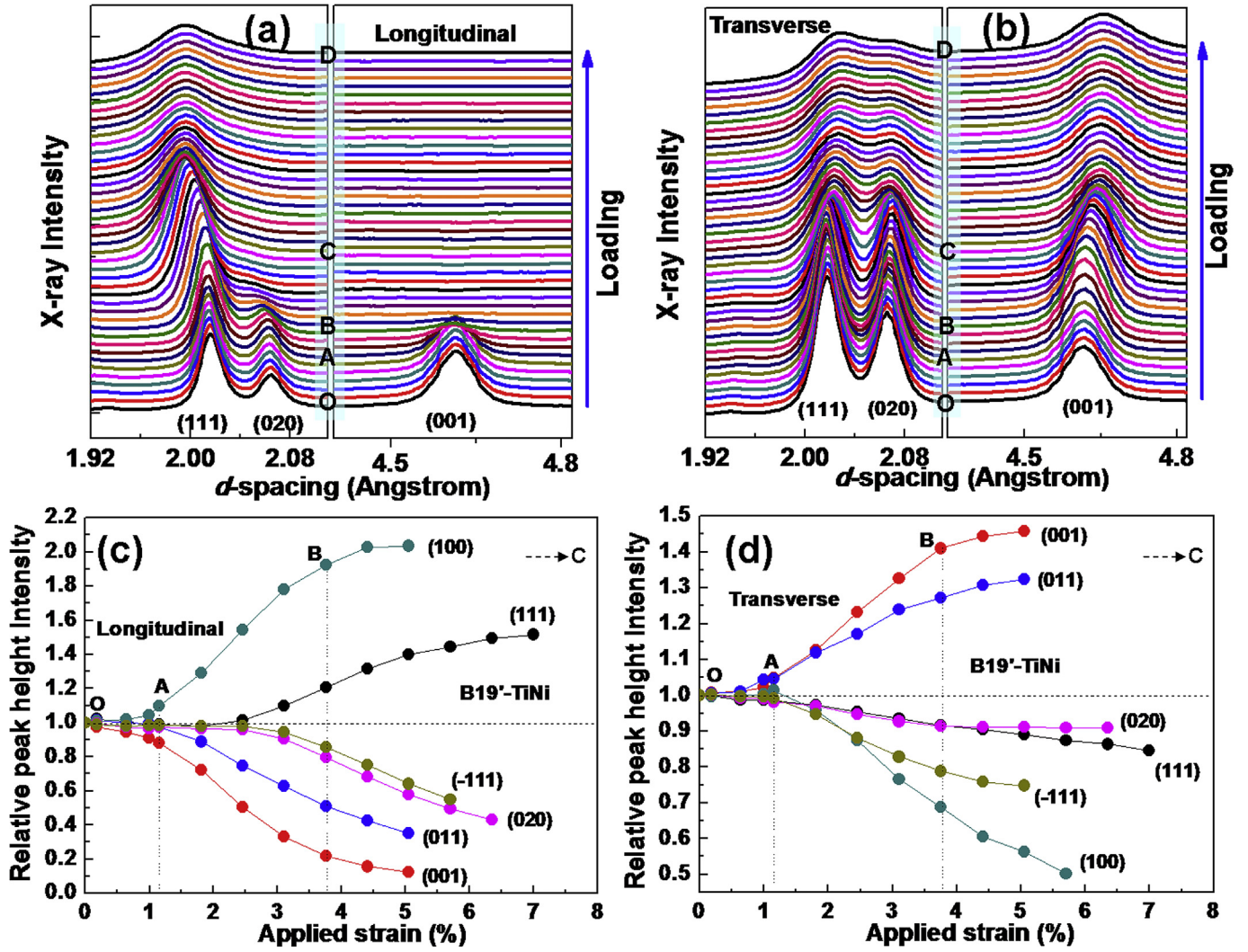

Fig. 6. Martensite variant reorientation of the TiNi matrix during compression. (a) 1D HR-XRD patterns demonstrating structural evolution during compression in the longitudinal direction (refer to Fig. 1, $\Phi = 90°$). (b) 1D HR-XRD patterns demonstrating structural evolution during compression in the transverse direction (refer to Fig. 1, $\Phi = 0°$). (c) Evolutions of the relative peak height intensities upon loading as a function of the applied strain in the longitudinal direction. (d) Evolutions of the relative peak height intensities upon loading as a function of the applied strain in the Transverse direction. Labels "O"-"D" in Fig. 7 correspond to the labels marked on the stress-strain curve of the composite shown in Fig. 5(a).

direction (Fig. 6(d)), the opposite behavior is observed, with the exception of ($\bar{1}$ 11) and (020). This implies that martensite variant reorientation occurred such that martensitic variants with (100) and (111) planes perpendicular to the loading direction grew at the expense of variants with ($\bar{1}$ 11), (020), (011) and (001) planes perpendicular to the loading direction. It is evident that the relative peak height intensities changed mainly in stage A-B, demonstrating that martensite variant reorientation occurs mainly during this stage. Massive martensite reorientation leads to the arrest of the lattice strain, as shown by the plateau in the B19′-TiNi (111) lattice strain curve in Fig. 5(a).

To further explore the deformation behavior of the TiNi matrix during the process of deformation, TiNi (001) diffraction, which has no overlap with other diffractions, is selected for further analysis. The 2D HE-XRD diffraction patterns of B19′-TiNi (001) at different applied strains were unrolled along the azimuthal angle from 0° to 360° and displayed in Fig. 7(a). The x-axis represents d-spacing. At 0% applied strain, the B19′-TiNi (001) diffraction line (ring) is continuous and straight, indicating an isotropic and stress-free state. With increasing the applied strain, the diffraction line broke up into two main sections centered around 0° and 180° (i.e., in the transverse direction) during stage A-B (1.2–3.9% strain), demonstrating martensite variant reorientation. Further increasing the applied strain to above 11.2% (in stage C-D) caused apparent curving and broadening of the diffraction "lines" into "banana" shapes, indicating lattice strain inhomogeneity. The curving of the diffraction lines indicates that the transverse direction (0° and 180°) experiences maximum tension and the longitudinal direction (90° and 270°) experiences maximum compression.

It is also evident that the length of the "banana-shaped" B19′-TiNi (001) diffraction lines shrunk (converges toward 0°/180°) during stage B-C and expanded during stage C-D. The convergence of the diffraction lines in stage B-C implies further variant alignment via reorientation toward the transverse direction after the apparent lattice strain plateau shown in Fig. 5(a). The angular expansion of the diffraction lines during stage C-D is attributed to excessive plastic deformation, which caused scattering of the otherwise near perfect crystal orientation alignment of the martensite. Meanwhile, it can be seen that the diffraction intensity along the angular section remained almost homogeneous in stage B-C, as shown in Fig. 7(b). Although the breadth of the "banana-shaped" diffraction lines expanded during stage C-D (Fig. 7(a)), the

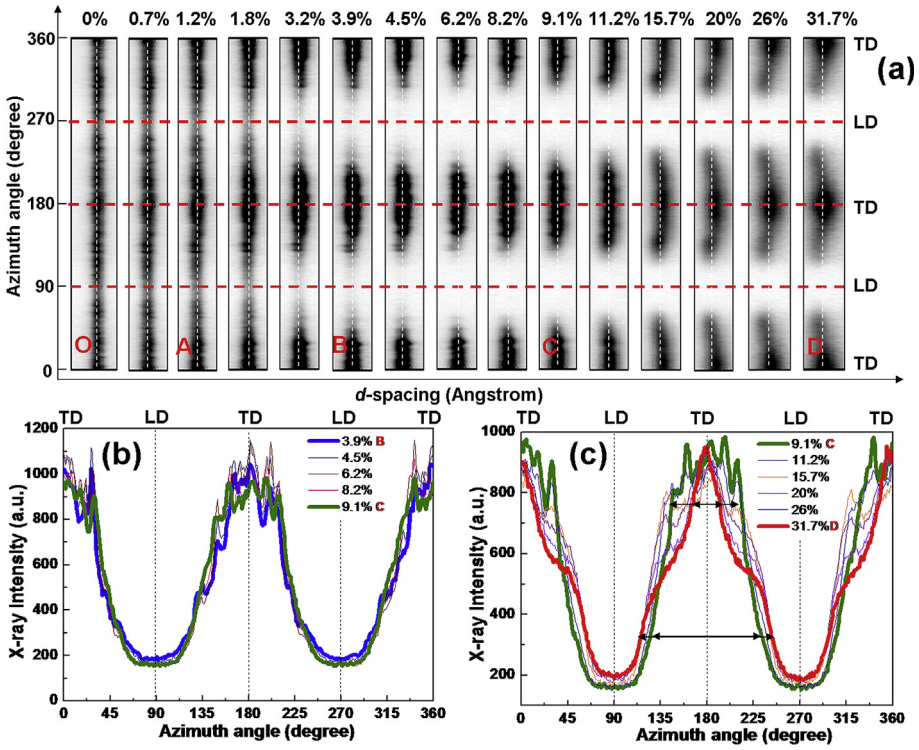

Fig. 7. Microscopic deformation behavior of TiNi during deformation. (a) The unrolled B19′-TiNi (001) diffraction along the full azimuthal circle (0°–360°) at different applied strains. The curvature of the diffraction lines indicates the stress state anisotropy of the sample. The transverse direction (TD) experienced maximum tension and the longitudinal direction (LD) experienced maximum compression. (b) B19′-TiNi (001) diffraction intensity versus azimuth angle at different applied strains in stage B-C. (c) B19′-TiNi (001) diffraction intensity versus azimuth angle at different applied strains in stage C-D.

diffraction intensity converged further to the center of the "banana-shaped" diffraction lines (Fig. 7(c)). This indicates continued martensite variant reorientation during the stage of plastic deformation of TiNi.

Fig. 8 shows the intensity distributions along the azimuth angle of B19′-TiNi (100), B19′-TiNi (020), B19′-TiNi (001), and B19′-TiNi (001) diffractions at 0%, 9.1%, and 31.7% of applied strains. At 0% strain, the diffraction intensities of (100) (Fig. 8(a)), (020) (Fig. 8(b)), and (011) (Fig. 8(d)) distributed practically uniformly along the azimuth circle, and that of (001) planes showed a weak preferential orientation towards the transverse direction (0°/180°). At 9.1% strain (corresponding to point C on the stress-strain curve shown in Fig. 4(a)), the preferential orientation of (001) planes in the transverse direction was intensified and the (100), (020), and (011) planes also developed clear preferential orientations. The (100) planes displayed the maximum intensities in the longitudinal direction (90°/270°). The (020) and (011) planes displayed the maximum intensities in the transverse direction (0°/180°). After deformation to 31.7% strain (corresponding to point D on the stress-strain curve shown in Fig. 4(a)), the preferential orientation of (001) planes converged further to the transverse direction. The intensity distributions of the (011) diffraction spitted into two peaks, and the maximum intensities of (011) changed from the 0°/180° to 0 ± 30° and 180 ± 30°. Due to overlap with other diffractions, the intensity distributions of (100) and (020) along the azimuth angle cannot be integrated and thus are not presented here.

3.5. Deformation of the hard Ti_3Sn component

The deformation behavior of the hard Ti_3Sn lamellar plates in the composite is analyzed using the Ti_3Sn (100) diffraction. The 2D HE-XRD Ti_3Sn (100) diffraction patterns collected at different applied strains are displayed along the azimuthal angle in Fig. 9(a). Prior to deformation (0% applied strain), the diffraction line (ring) is straight and continuous, indicating stress-free and isotropic state. Upon compression, the diffraction line became curved and then discontinuous at higher strain levels. The curved diffraction line indicates lattice strain anisotropy along the azimuthal circle, with the maximum "compression" occurring in the longitudinal direction (90°/270°) and the maximum "tension" occurring in the transverse direction (0°/180°).

The breakdown of the continuity of the diffraction line indicates preferential crystal plane rotation induced by the deformation. Fig. 9(b) shows the diffraction intensity distribution of Ti_3Sn (100) along the azimuth angle. It is seen that the magnitude of diffraction intensity variation increased progressively with increasing the applied strain. The diffraction intensity anisotropy, defined as the diffraction intensity variation magnitude ΔI relative to the mean intensity I_0, which is a measure of the degree of texture, is shown in Fig. 9(c) as a function of the applied strain. It is seen that the Ti_3Sn (100) diffraction intensity anisotropy remained almost constant in the initial stage of deformation, and then increased continuously with increasing the applied strain. The significant orientation change, thus the anisotropy, is not expected for Ti_3Sn, since it experiences no variant reorientation. This is attributed to rigid body rotation of the Ti_3Sn plates.

Fig. 10 shows diffraction intensity distributions along the azimuth angle of Ti_3Sn (100), Ti_3Sn (002) and Ti_3Sn (110) planes before and after the deformation. Prior to the deformation (0% strain), all four planes showed almost uniform distribution along the azimuthal ring. After the deformation (31.7%), the (100) plane developed clear preferential orientation in the transverse direction (at 0° and 180°). The (002) plane showed preferential orientations in six directions at 0°, 0 ± 50°, 180°, and 180 ± 50°. The (110) plane

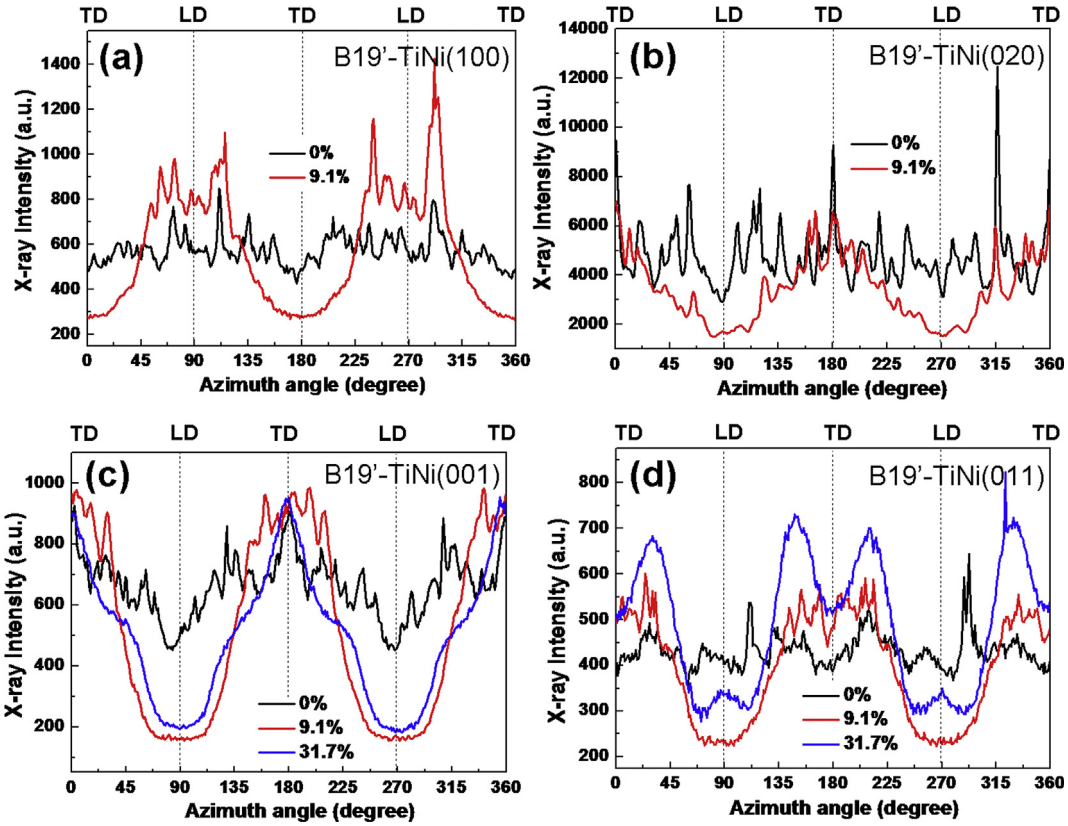

Fig. 8. TiNi diffraction intensity distribution along the azimuth circle at 0%, 9.1%, and 31.7% strains. (a) B19′-TiNi (100). (b) B19′-TiNi (020). (c) B19′-TiNi (001). (d) B19′-TiNi (011).

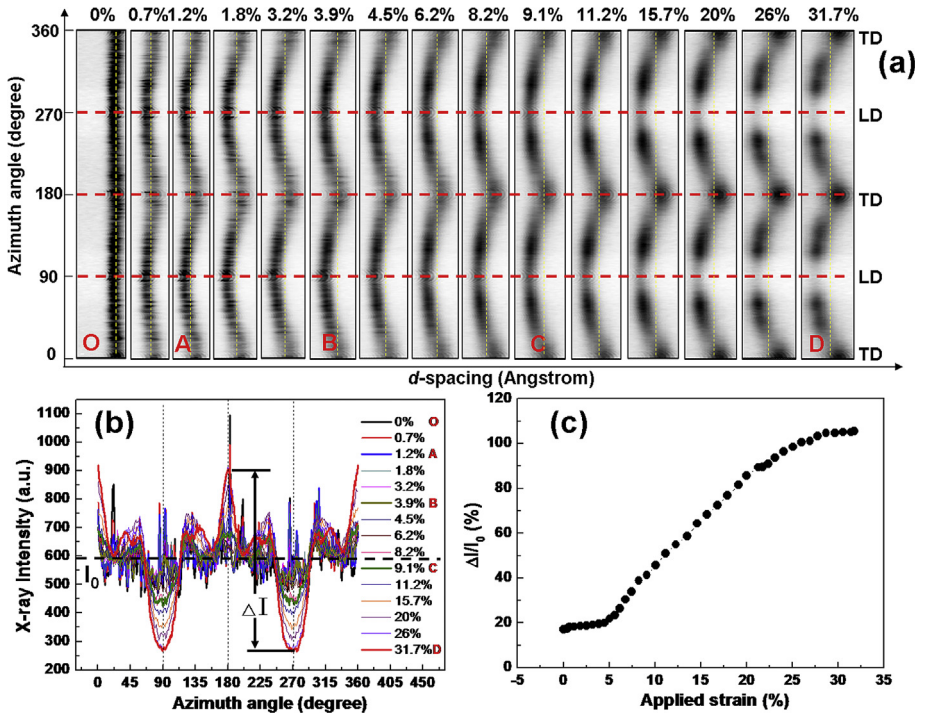

Fig. 9. Microscopic deformation behavior of Ti_3Sn during deformation. (a) The unrolled Ti_3Sn (100) diffraction along the full azimuth circle (0°–360°) at different applied strains. The curvature of the diffraction lines indicates the stress state anisotropy of the sample. The transverse direction (TD) experienced maximum tension and the longitudinal direction (LD) experienced maximum compression. (b) Ti_3Sn (100) diffraction intensity versus azimuth angle at different applied strains. (c) Evolution of Ti_3Sn (100) diffraction intensity anisotropy during loading.

developed clear preferential orientation in the longitudinal direction (at 90° and 270°) and secondary orientations in four other directions at 0 ± 30° and 180 ± 30°. It is interesting to note that both (100) and (002) developed preferential orientation along the transverse direction (0°/180°). It is known that for the D019 (ordered hexagonal-close-packed) crystal structure of Ti_3Sn, (100) and (002) are perpendicular to each other. This implies that the observed texture of Ti_3Sn is not crystallography-based but due to other reasons, in this case grain rotation, i.e. a grain geometric texture.

4. Discussion

4.1. Martensite variant reorientation and texture formation in TiNi matrix

It is evident in Figs. 6 and 8 that the B19′-TiNi matrix developed clear texture upon compression deformation. The main features observed of the texture are summarized in Table 1. The [100]* alignment to the loading direction and [001]* and [020]* to the transverse direction are attributed to the edge length asymmetry of the B19′-TiNi unit cell. In TiNi, B19' [100], B19' [010] and B19' [001] correspond to the B2 [001], B2 [110] and B2 [$\bar{1}$ 10], respectively. The lengths of the basic vectors of the B19′-TiNi unit cell are 0.289 nm for the *a* axis ([100] vector), 0.291 nm for the *b* axis ([010] vector), and 0.327 nm for the *c* axis ([001] vector). The *a* axis is the shortest and the *c* axis is the longest [38,39]. Thus upon compression, variants with the *c* axis aligned perpendicular to the loading direction and the *a* axis aligned parallel with the loading direction tend to grow at the expense of other variants, apparently in order to achieve the maximum crystal orientation-associated deformation in the loading direction. This preferential orientation is schematically represented by the grain expressed by the red vectors shown in Fig. 11. Considering that the compressed sample has a planar isotropy in the plane perpendicular to the loading direction, these grains have their three basic vectors located on the surfaces of the cones formed by spinning the red vectors around the Z-axis. This implies that in XRD these grains will feature (001) and (020) diffractions at 0° and 180° azimuthal angles and (100) at near 90° (83.2°) on the Debye ring (the large circle on the page plane). Apparently, the expected XRD texture from such a texture is consistent with the experimental observations shown in Fig. 8(a)–(d).

The observed [011]* texture requires more analysis. The [011]* vector is at 48° from [001]* but also has an azimuthal angle of 0°, as indicated by the green vectors in Fig. 11. This implies that for the preferential orientation texture expressed by the red vectors, the (011) diffraction is expected at the transverse direction. This is consistent with the observation made after 9.1% strain, as seen in Fig. 8(d). However, after further deformation to 31.7% strain, the (011) diffraction maxima at 0° and 180° each split into double maxima 0 ± 30° and 180 ± 30° (Fig. 8(d)). This stage of deformation corresponds to stage CD on the stress-strain curve shown in Fig. 4(a) and stage CD on the lattice strain curve shown in Fig. 5(a), i.e., dominantly plastic deformation via dislocation slip. This implies that the further change of (011) preferential orientation from 0°/180° to 0 ± 30° and 180 ± 30° is caused by plastic deformation.

From the above analysis, it is clear that all the preferential orientations observed reflect the same texture which can be described by the radiating distribution of [001]* in the transverse plane to the loading direction. Another observation to note is that [001]*transverse texture continued to develop during plastic deformation (stage CD) well beyond the end of the apparent plateau for variant reorientation (stage AB), as seen in Fig. 7(c).

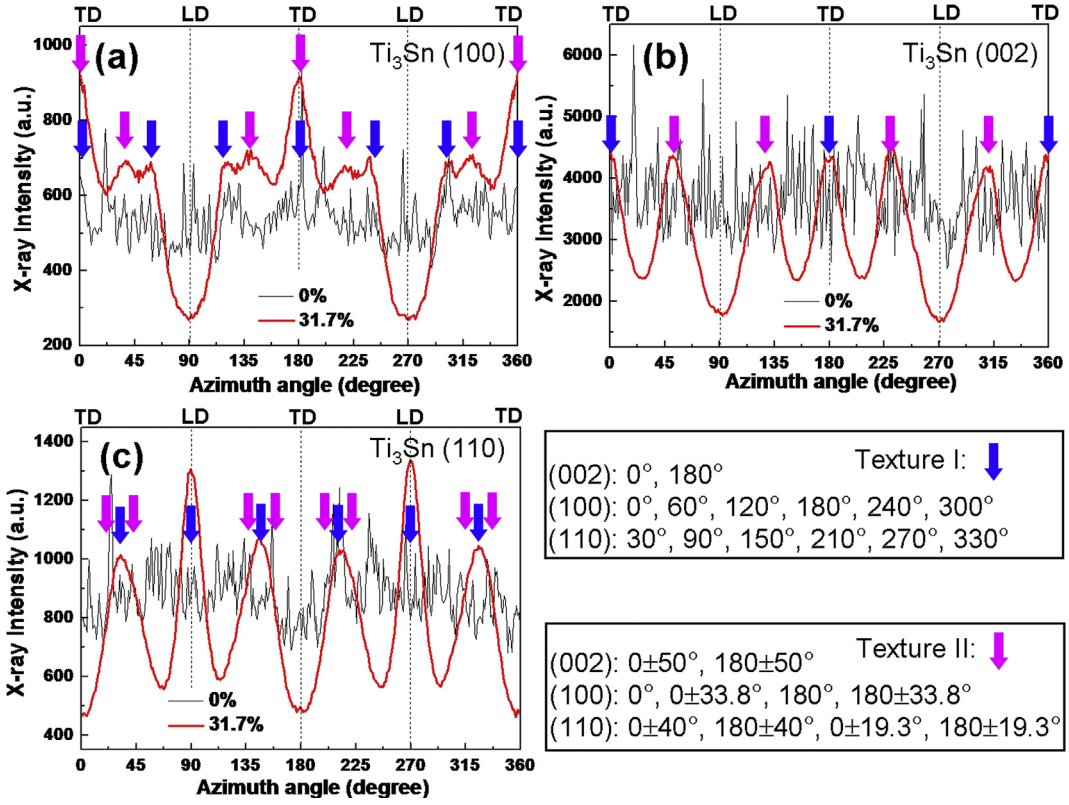

Fig. 10. Ti_3Sn diffraction intensity distribution along the azimuth circle at 0% and 31.7% strains. (a) Ti_3Sn (100). (b) Ti_3Sn (002). (c) Ti_3Sn (110).

Table 1
B19′-TiNi matrix and Ti_3Sn texture observations.

B19′-TiNi matrix	Crystallographic directions	[100]*	[020]*	[001]*	[011]*
	Azimuthal angle	90°, 270°	0°, 180°	0°, 180°	0 ± 30°, 180 ± 30°
Ti_3Sn plates	Crystallographic directions	[100]*	[002]*	[110]*	
	Azimuthal angle	0°, 180°	0°, 0 ± 50°, 180°, 180 ± 50°	0 ± 30°, 180 ± 30°, 90°, 270°	

4.2. Texture formation of hard Ti_3Sn by rigid rotation

It is also evident in Figs. 9 and 10 that Ti_3Sn also developed clear texture after the deformation. The texture manifests as a preferential alignment of (110) (Fig. 10(c)) and avoidance of (100) (Fig. 10(a)) and (002) (Fig. 10(b)) along the compression axis (90°/270° azimuthal angle), as summarized in Table 1.

Ti_3Sn is a brittle intermetallic compound. It does not have enough effective slip systems in its D019 crystal structure [31,40], thus lacks a plausible mechanism to develop texture by plastic deformation. A feasible mechanism is rigid body rotation of the Ti_3Sn eutectic lamellae. The Ti_3Sn eutectic lamellae were observed to generally have a preferential plate orientation of (110) along their normal direction, as confirmed by TEM and SAED observations (Fig. 3(b)) and schematically expressed in Fig. 12(d). In the D019 Ti_3Sn hexagonal structure (c/a = 0.805), (110) is the close packed plane and [$\bar{1}$ 11], which is inside the (110) plane, is the close packed direction. Thus formation of (110) Ti_3Sn lamellae helps to minimize the interface energy in the eutectic structure and to maximize the growth rate along the lateral directions of the lamella plates. The excessive deformation of the TiNi matrix, including both the martensite reorientation and plastic deformation, facilitates the rigid body rotation [41] of the Ti_3Sn eutectic lamellae to produce a physical texture of the Ti_3Sn plates in the composite.

Fig. 12 presents a schematic of this lamella rotation under compression and spatial preferential orientation of Ti_3Sn. Prior to deformation, the eutectic lamellae are randomly distributed and have an isotropic microstructure (neglecting solidification texture of small ingots), as schematically expressed in Fig. 12(a). During deformation, the Ti_3Sn lamellae gradually rotate to align to the transverse plane to the loading direction, as depicted in Fig. 12(b). The correspondence between the geometric shape and the crystallographic orientation of the Ti_3Sn lamellae is shown in Fig. 12(d). The condition of diffraction of the Ti_3Sn lamellae such oriented in Fig. 12(b) is expressed in Fig. 12(e). For the texture expressed in Fig. 12(d), the [002]* diffraction (the red vectors) appears at 0° and 180° on the Debye ring. The [110]* vectors (the pink vectors) and [100]* vectors (the green vectors) are expected to appear at 30° and 60° azimuthal angles, respectively.

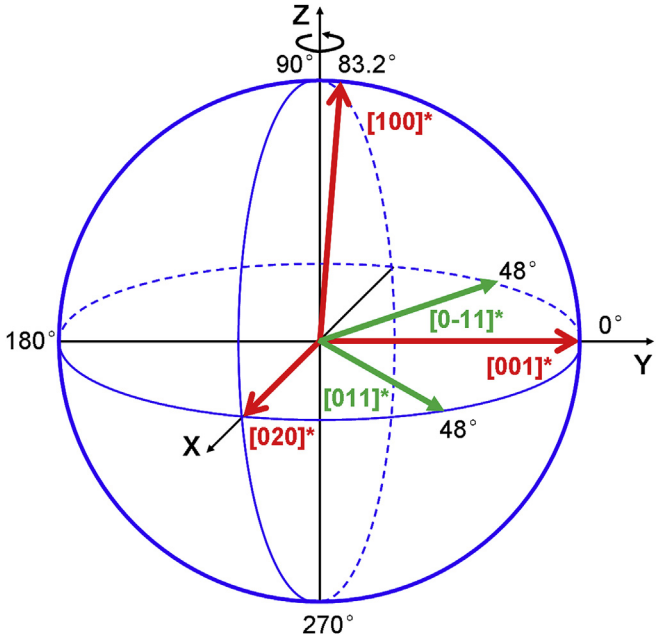

Fig. 11. Schematic representation of spatial preferential orientation of B19′-TiNi. The paper plane is the plane of the Debye ring for diffraction.

However, referring to the experimental evidence presented in Fig. 10, it is seen that the experimental observations do not quite agree with these expectations, particularly for (002) diffraction. The (002) plane showed preferential orientation in six directions at 0°, (approximately) 0 ± 50°, 180°, and 180 ± 50°. For D019 crystal structure, only two (002) diffractions at antipode positions are expected for a unique texture. The observation of 6 clear diffraction maxima indicates explicitly that there exists more than one texture (in fact two). Further examination of the evidence presented in Fig. 10 also indicates that the 6 diffraction intensity maxima are not equally spaced on the Debye ring and that the maxima peak profiles at approximately 0 ± 50° and 180 ± 50° are not symmetric. These further imply that the preferential orientations are from different groups of grains, i.e., there co-exist two Ti_3Sn textures within the matrix. Texture I refers to the Ti_3Sn grains with their [002]* aligned in 0/180° on the Debye ring, as indicated by the set of blue arrows in Fig. 10. Texture II refers to the grains having their [002]* lying at around 0 ± 50° and 180 ± 50° azimuthal angles on the Debye ring. Texture II of the Ti_3Sn lamellae is schematically shown in Fig. 12(f), which is produced by rotating Texture I about the X axis anticlockwise by 50°. In this case, the [100]* vectors are tilted to 0 ± 33.8° and 180 ± 33.8° azimuth angles and the [110]* vectors are at 0 ± 19.3° and 180 ± 19.3° azimuth angles. The expected diffraction intensity maxima positions for texture II are indicated by the pink arrows in Fig. 10. It is evident that these expectations are agreeable with the experimental observations.

The reason for the occurrence of Texture II is unclear. It may be related to the two distinctive morphologies of the eutectic structure seen in Fig. 2(a). It is easy to understand that not all Ti_3Sn lamellae can be fully rotated as per texture I. This may be explained as expressed in Fig. 12(c). The Ti_3Sn lamellae are closely placed with narrow gaps of TiNi in between. Deformation of the soft TiNi allows the Ti_3Sn lamellae to rotate in orientations, but only so much till the Ti_3Sn plates come into contact with one another (in reality the rotation should be even less because the TiNi cannot be totally deformed to nil thickness). Obviously the arrest angle of the rotation of the Ti_3Sn plates is dependent on the lamellae thickness, spacing and the deformability of the soft TiNi phase.

4.3. The principle of "lattice strain matching" and large elastic strains of the brittle Ti_3Sn

It is evident in Fig. 5(a) that the elastic strain of hard Ti_3Sn phase reached 1.95%. This is far greater than the maximum elastic strains of bulk Ti_3Sn reported in the literature, which is approximately 0.3% [31]. This elastic strain achieved in the composite is more than six times of what is possible conventionally in bulk Ti_3Sn. In addition, this elastic strain value is also significantly higher than the elastic

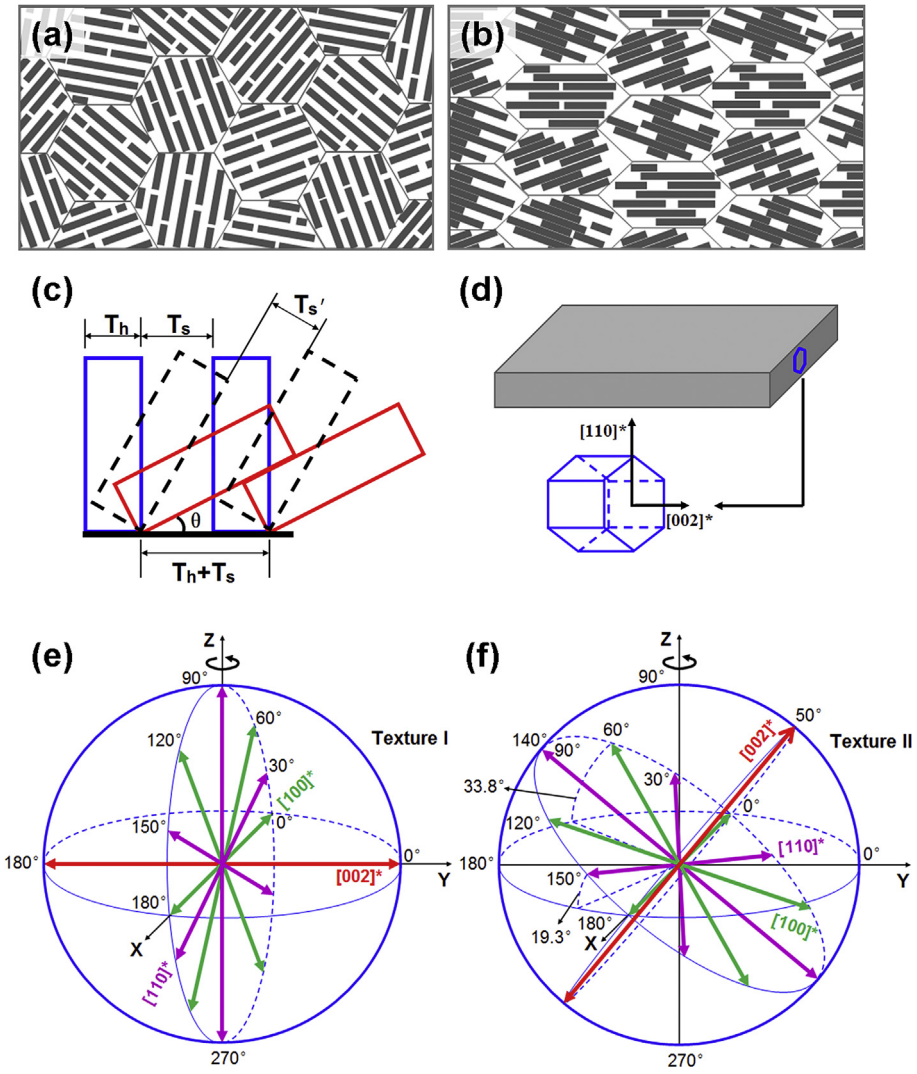

Fig. 12. Schematic representation of lamellae rotation and spatial preferential orientation. (a) The 2-D eutectic lamellar structure before deformation. (b) The 2-D eutectic lamellar structure after deformation. (c) Lamellae rotation results in the rigid Ti_3Sn contacting together. T_h and T_s are the lamellae thickness of hard Ti_3Sn and soft TiNi, respectively. (d) The crystal orientation of Ti_3Sn lamella. (e) and (f) are the spatial preferential orientation of Ti_3Sn. The paper plane is the plane of the Debye ring for diffraction.

strains of many other hard inclusions (including nanowires, lamellae and particles) embedded in conventional metal matrices that deform by dislocation slip (Fig. 5(b)). This exceptionally high elastic strain of Ti_3Sn, which implies exceptionally large strength contribution, is attributed to the effect of "lattice strain matching" between the martensitic TiNi matrix and the hard and brittle Ti_3Sn inclusions in the composite. This effect was first demonstrated in a NiTi-Nb nanowire composite in which the Nb nanowires achieved an exceptionally large elastic strain of above 6%, enabled by the phase transforming NiTi matrix [19,20]. This work further demonstrates that lattice strain matching mechanism also occurs for brittle inclusions like Ti_3Sn.

The working mechanism of the lattice strain matching may be explained as following. The martensitic transformation or martensite variant reorientation in the TiNi matrix produces a uniform lattice distortion strain of several percent (e.g., ~7%) [19,20,38], which is compatible to the uniform lattice dilatation elastic strains expected of the nanoinclusions. This allows effective load transfer from the matrix to the nanoinclusions. In comparison, the situation of lattice distortion is fundamentally different for dislocation slip occurring in conventional metals [38,42,43]. In this case, the lattice distortion is highly localized, reaching to a nominal ~100% at the site of a dislocation line whereas remaining well below 1% in other areas away from a dislocation line [19,20,42].

This concept is schematically expressed in Fig. 13, as for the situation of a nominal 3% global tensile strain. The horizontal axis represents a spatial dimension along the interface in the composite and the vertical axis expresses the magnitude of lattice distortion. Fig. 13(a) represents the case of a composite with a dislocation slip matrix and Fig. 13(b) represents the case of a composite with a martensitic phase transforming matrix. In the former case, the expected elastic strain of the hard phase nanoinclusion is at 3% (if it were standing alone). The lattice strain distribution in the matrix is shown as the blue curve. The highly localized lattice distortion at a dislocation exerts high local stress concentration and triggers premature failure of the nanoinclusion, thus preventing it from reaching high elastic strains. In contrast, in the latter case (Fig. 13(b)), the matrix undergoes a partial martensitic phase transformation or variant reorientation, with a lattice distortion distribution as shown by the blue curve. It is thus free of high local stress concentrations and allows a lattice distortion match between the uniform elastic lattice strain of the nanoinclusion and the

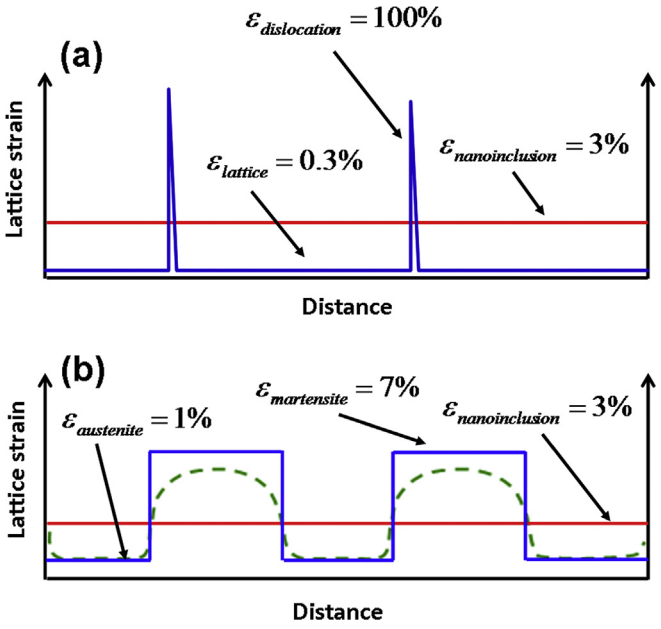

Fig. 13. Lattice strain schematic representation of different composite. (a) Dislocation slip matrix composite. (b) Phase transforming matrix composite.

martensitic transforming matrix at the interface, as expressed by the green curve. This effect of "lattice strain matching" allows effective load transfer from the matrix to the nanoinclusion and encourages its high elastic straining during deformation. High elastic strains imply high load bearing contribution, thus ensuring the high strength of the composite.

5. Conclusions

This study analyzed the microscopic deformation behavior of a hard-soft dual phase Ti_3Sn/TiNi eutectic composite by means of in situ synchrotron high-energy X-ray diffraction during compression. The main findings are summarized as follows:

The composite has an ultrafine lamella and isotropic eutectic cell microstructure. Under compression at room temperature, the composite exhibits a high strength of 3 GPa and a large fracture strain exceeding 30%. These values are significantly higher than those of other similar hard-soft dual phase eutectic composites in which the soft component is a conventional metal (i.e. deforms primarily via dislocation slip).

Upon deformation, the soft TiNi matrix deformed via martensite variant reorientation. The martensite variant reorientation process created a strong crystallographic texture of (001) along the compression axis, and is also found to continue well into the stage of plastic deformation of TiNi.

The hard Ti_3Sn lamellae deformed predominantly via rigid body rotation as well as elastic deformation, producing a preferred alignment of lamellae as well as a crystallographic texture.

The hard Ti_3Sn is also found to produce an exceptionally large elastic strain of 1.95% in the composite, which implies high load bearing contribution to the strength of the composite. This elastic strain is significantly higher than that achieved in free standing bulk Ti_3Sn and the elastic strains achieved in other hard inclusions embedded in composites with conventional metal matrices that deform by dislocation slip. This is attributed to the effective lattice strain matching between the martensitic transformation lattice distortion of the TiNi matrix and the elastic strains of Ti_3Sn lamellae.

Acknowledgements

This work was supported by the National Natural Science Foundation of China (NSFC) (Grant No. 51601069, 51231008 and 11474362), the Australian Research Council (Grant No. DP160105066 and DP140103805) and the Natural Science Foundation of Jiangsu Province (Grant No. BK20160514). The use of the Advanced Photon Source was supported by the US Department of Energy, Office of Science, and Office of Basic Energy Science, Office of Basic Energy Sciences, under Contract No. DE-AC02-06CH11357.

References

[1] Y. Yue, P. Liu, Z. Zhang, X. Han, E. Ma, Approaching the theoretical elastic strain limit in copper nanowires, Nano Lett. 11 (2011) 3151–3155.
[2] G. Richter, K. Hillerich, D.S. Gianola, R. Monig, O. Kraft, C.A. Volkert, Ultrahigh strength single crystalline nanowhiskers grown by physical vapor deposition, Nano Lett. 9 (2009) 3048–3052.
[3] K. Koziol, J. Vilatela, A. Moisala, M. Motta, P. Cunniff, M. Sennett, A. Windle, High-performance carbon nanotube fiber, Science 318 (2007) 1892–1895.
[4] S.H. Xia, J.T. Wang, A micromechanical model of toughening behavior in the dual-phase composite, Int. J. Plast. 26 (2010) 1442–1460.
[5] T.J.A. Doel, P. Bowen, Tensile properties of particulate-reinforced metal matrix composites, Compos. Part A Appl. S 27 (1996) 655–665.
[6] Z. Tan, Z. Chen, G. Fan, G. Ji, J. Zhang, R. Xu, R. Xu, A. Shan, Z. Li, D. Zhang, Effect of particle size on the thermal and mechanical properties of aluminum composites reinforced with SiC and diamond, Mater. Des. 90 (2016) 845–851.
[7] X. Guo, Q. Guo, Z. Li, G. Fan, D.B. Xiong, Y. Su, J. Zhang, C.L. Gan, D. Zhang, Interfacial strength and deformation mechanism of SiC–Al composite micropillars, Scr. Mater. 114 (2016) 56–59.
[8] G. He, J. Eckert, W. Löser, L. Schultz, Novel Ti-base nanostructure–dendrite composite with enhanced plasticity, Nat. Mater. 2 (2003) 33–37.
[9] D.C. Hofmann, J.Y. Suh, A. Wiest, G. Duan, M.L. Lind, M.D. Demetriou, W.L. Johnson, Designing metallic glass matrix composites with high toughness and tensile ductility, Nature 451 (2008) 1085–1089.
[10] J.W. Qiao, T. Zhang, F.Q. Yang, P.K. Liaw, S. Pauly, B.S. Xu, A tensile deformation model for in-situ dendrite/metallic glass matrix composites, Sci. Rep. 3 (2013) 2816.
[11] Z. Li, K.G. Pradeep, Y. Deng, D. Raabe, C.C. Tasan, Metastable high-entropy dual-phase alloys overcome the strength–ductility trade-off, Nature 534 (2016) 227–230.
[12] V.Y. Mehr, M.R. Toroghinejad, A. Rezaeian, Mechanical properties and microstructure evolutions of multilayered Al–Cu composites produced by accumulative roll bonding process and subsequent annealing, Mater. Sci. Eng. A 601 (2014) 40–47.
[13] Y. Flom, R.J. Arsenault, Deformation of SiC/Al composites, JOM 38 (1986) 31–34.
[14] M.L. Young, R. Rao, J.D. Almer, D.R. Haeffner, J.A. Lewis, D.C. Dunand, Effect of ceramic preform geometry on load partitioning in Al_2O_3–Al composites with three-dimensional periodic architecture, Mater. Sci. Eng. A 526 (2009) 190–196.
[15] L. Wang, M. Li, J. Almer, Investigation of deformation and microstructural evolution in Grade 91 ferritic–martensitic steel by in situ high-energy X-rays, Acta Mater. 62 (2014) 239–249.
[16] M.L. Young, J. DeFouw, J.D. Almer, D.C. Dunand, Load partitioning during compressive loading of a Mg/MgB_2 composite, Acta Mater. 55 (2007) 3467–3478.
[17] M.L. Young, J.D. Almer, M.R. Daymond, D.R. Haeffner, D.C. Dunand, Load partitioning between ferrite and cementite during elasto-plastic deformation of an ultrahigh-carbon steel, Acta Mater. 55 (2007) 1999–2011.
[18] D.H. Bacon, L. Edwards, J.E. Moffatt, M.E. Fitzpatrick, Synchrotron X-ray diffraction measurements of internal stresses during loading of steel-based metal matrix composites reinforced with TiB_2 particles, Acta Mater. 59 (2011) 3373–3383.
[19] S. Hao, L. Cui, D. Jiang, X. Han, Y. Ren, J. Jiang, Y. Liu, Z. Liu, S. Mao, Y. Wang, Y. Li, X. Ren, X. Ding, S. Wang, C. Yu, X. Shi, M. Du, F. Yang, Y. Zheng, Z. Zhang, X. Li, D.E. Brown, J. Li, A transforming metal nanocomposite with large elastic strain, low modulus, and high strength, Science 339 (2013) 1191–1194.
[20] S. Hao, L. Cui, H. Wang, D. Jiang, Y. Liu, J. Yan, Y. Ren, X. Han, D.E. Brown, J. Li, Retaining large and adjustable elastic strains of kilogram-scale Nb nanowires, ACS Appl. Mater. Inter 8 (2016) 2917–2922.
[21] K. Zang, S. Mao, J. Cai, Y. Liu, H. Li, S. Hao, D. Jiang, L. Cui, Revealing ultralarge and localized elastic lattice strains in Nb nanowires embedded in NiTi matrix, Sci. Rep. 5 (2015) 17530.
[22] D.V. Louzguine-Luzgin, A. Vinogradov, G. Xie, S. Li, A. Lazarev, S. Hashimoto, A. Inoue, High-strength and ductile glassy-crystal Ni-Cu-Zr-Ti composite exhibiting stress-induced martensitic transformation, Philos. Mag. 89 (2009) 2887–2901.
[23] S. Pauly, J. Das, J. Bednarcik, N. Mattern, K.B. Kim, D.H. Kim, J. Eckert, Deformation-induced martensitic transformation in Cu-Zr-(Al, Ti) bulk metallic glass composites, Scr. Mater. 60 (2009) 431–434.

[24] J. Das, K.B. Kim, F. Baier, W. Loser, J. Eckert, High-strength Ti-base ultrafine eutectic with enhanced ductility, Appl. Phys. Lett. 87 (2005), 161907–161907-3.
[25] J.M. Park, K.B. Kim, W.T. Kim, M.H. Lee, J. Eckert, D.H. Kim, High strength ultrafine eutectic Fe-Nb-Al composites with enhanced plasticity, Intermetallics 16 (2008) 642–650.
[26] J.M. Park, S.W. Sohn, T.E. Kim, D.H. Kim, K.B. Kim, W.T. Kim, Nanostructure-dendrite composites in the Fe-Zr binary alloy system exhibiting high strength and plasticity, Scr. Mater. 57 (2007) 1153–1156.
[27] J.M. Park, N. Mattern, U. Kühn, J. Eckert, K.B. Kim, W.T. Kim, K. Chattopadhyay, D.H. Kim, High-strength bulk Al-based bimodal ultrafine eutectic composite with enhanced plasticity, J. Mater. Res. 24 (2009) 2605–2609.
[28] Z. Hu, Y. Zhan, J. She, The role of Nd on the microstructural evolution and compressive behavior of Ti-Si alloys, Mater. Sci. Eng. A 560 (2013) 583–588.
[29] J.M. Park, D.H. Kim, K.B. Kim, M.H. Lee, W.T. Kim, J. Eckert, Influence of heterogeneities with different length scale on the plasticity of Fe-base ultrafine eutectic alloys, J. Mater. Res. 23 (2008) 2003–2008.
[30] D.H. Pi, G.A. Song, J.H. Han, J.M. Park, G.R. Lim, D.H. Kim, S. Yi, S.H. Yi, N.S. Lee, Y. Seo, K.B. Kim, Effect of Nb on microstructure and mechanical properties of ultrafine eutectic Fe-Ni-B-Si composites, J. Alloys Compd. 504S (2010) S487–S490.
[31] T. Hashimoto, M. Nakamura, S. Takeuchi, Plastic deformation of Ti_3Sn, Mater. Trans. JIM 31 (1990) 195–199.
[32] O. Muránsky, P. Šittner, J. Zrník, E.C. Oliver, In situ neutron diffraction investigation of the collaborative deformation-transformation mechanism in TRIP-assisted steels at room and elevated temperatures, Acta Mater. 56 (2008) 3367–3379.
[33] S. Roy, J. Gibmeier, A. Wanner, In situ study of internal load transfer in a novel metal/ceramic composite exhibiting lamellar microstructure using energy dispersive synchrotron x-ray diffraction, Adv. Eng. Mater. 11 (2009) 471–477.
[34] T.E. Wilkes, B.J. Harder, J.D. Almer, K.T. Faber, Load partitioning in honeycomb-like silicon carbide aluminum alloy composites, Acta Mater. 57 (2009) 6234–6242.
[35] N. Jia, Z.H. Cong, X. Sun, S. Cheng, Z.H. Nie, Y. Ren, P.K. Liaw, Y.D. Wang, An in situ high-energy X-ray diffraction study of micromechanical behavior of multiple phases in advanced high-strength steels, Acta Mater. 57 (2009) 3965–3977.
[36] C.C. Aydıner, D.W. Brown, N.A. Mara, J. Almer, A. Misra, In situ x-ray investigation of freestanding nanoscale Cu-Nb multilayers under tensile load, Appl. Phys. Lett. 94 (2009), 031906–031906-3.
[37] L. Thilly, S. Van Petegem, P.O. Renault, F. Lecouturier, V. Vidal, B. Schmitt, H. Van Swygenhoven, A new criterion for elasto-plastic transition in nanomaterials: application to size and composite effects on Cu-Nb nanocomposite wires, Acta Mater. 57 (2009) 3157–3169.
[38] K. Otsuka, X. Ren, Physical metallurgy of TiNi-based shape memory alloys, Prog. Mater Sci. 50 (2005) 511–678.
[39] D.C. Dunand, D. Mari, M.A.M. Bourke, J.A. Roberts, NiTi and NiTi-TiC composites: part IV. Neutron diffraction study of twinning and shape-memory recovery, Metall. Mater. Trans. A 27 (1996) 2820–2836.
[40] P.J. Jones, J.W. Edington, Slip systems in the intermetallic compound Ti_3Sn, Philos. Mag. 27 (1973) 393–404.
[41] L. Margulies, G. Winther, H.F. Poulsen, In situ measurement of grain rotation during deformation of polycrystals, Science 291 (2001) 2392–2394.
[42] S. Ogata, J. Li, S. Yip, Ideal pure shear strength of aluminum and copper, Science 298 (2002) 807–811.
[43] J. Zhang, L. Cui, D. Jiang, Y. Liu, S. Hao, Y. Ren, X. Han, Z. Liu, Y. Wang, C. Yu, Y. Huan, X. Zhao, Y. Zheng, H. Xu, X. Ren, X. Li, A biopolymer-like metal enabled hybrid material with exceptional mechanical prowess, Sci. Rep. 5 (2015) 8357.